UNIVERSITY OF LEEDS

This is a repository copy of *Analysis of fracture induced scattering of microseismic shear-waves*.

White Rose Research Online URL for this paper:
http://eprints.whiterose.ac.uk/115103/

Version: Accepted Version

Article:
Yousef, BM and Angus, DA orcid.org/0000-0003-0734-7835 (2017) Analysis of fracture induced scattering of microseismic shear-waves. Studia Geophysica et Geodaetica, 61 (4). pp. 728-753. ISSN 0039-3169

https://doi.org/10.1007/s11200-016-0384-9

© 2017 Inst. Geophys. CAS, Prague. This is an author produced version of an article published in Studia Geophysica et Geodaetica. The final publication is available at Springer via https://doi.org/10.1007/s11200-016-0384-9. Uploaded in accordance with the publisher's self-archiving policy.

Reuse
Items deposited in White Rose Research Online are protected by copyright, with all rights reserved unless indicated otherwise. They may be downloaded and/or printed for private study, or other acts as permitted by national copyright laws. The publisher or other rights holders may allow further reproduction and re-use of the full text version. This is indicated by the licence information on the White Rose Research Online record for the item.

Takedown
If you consider content in White Rose Research Online to be in breach of UK law, please notify us by emailing eprints@whiterose.ac.uk including the URL of the record and the reason for the withdrawal request.

White Rose university consortium
Universities of Leeds, Sheffield & York

eprints@whiterose.ac.uk
https://eprints.whiterose.ac.uk/

Analysis of fracture induced scattering of microseismic shear-waves

Yousef, B.M. & Angus, D.A.*

School of Earth & Environment, University of Leeds, Leeds, LS2 9JT, UK

Now at: ESG Solutions, Kingston, Canada

Corresponding author: Doug Angus, doug.angus@esgsolutions.com

Abstract

Fractures are pervasive features within the Earth's crust and have a significant influence on the multi-physical response of the subsurface. The presence of coherent fracture sets often leads to observable seismic scattering enabling seismic techniques to remotely locate and characterise fracture systems. In this study, we confirm the general scale-dependence of seismic scattering and provide new results specific to shear-wave propagation. We do this by generating full waveform synthetics using finite-difference wave simulation within an isotropic background model containing explicit fractures. By considering a suite of fracture models having variable fracture density and fracture size, we examine the widening effect of wavelets due to scattering within a fractured medium by using several different approaches, such as root-mean-square envelope analysis, shear-wave polarisation distortion, differential attenuation analysis and peak frequency shifting. The analysis allows us to assess the scattering behaviour of parametrised models in which the propagation direction is either normal or parallel to the fracture surfaces. The quantitative measures show strong observable deviations for fractures size on the order of or greater than the dominant seismic wavelength within the Mie and geometric scattering regime for both propagation normal and parallel to fracture strike. The results suggest that strong scattering is symptomatic of fractures having size on the same order of the probing seismic wave.

Keywords: explicit fractures, finite-difference, full-waveform synthetics, scattering, shear-wave

1. Introduction

Fractures within the Earth's crust range in size over several orders of magnitude, from large-scale faults (100 kms) observed on the Earth's surface down to micro-cracks (μm) observed in core samples. Since fractures are prevalent features in the subsurface and vary in size over several orders of magnitude (e.g., 1), they play a critical role in the multi-physical response of the Earth, controlling not only the mechanical and fluid-flow properties but also the geophysical response. For geo-industrial applications, fractures can have a significant influence on the integrity of mine excavations, boreholes and the caprock integrity of reservoirs and their ability for maintaining barriers between potable water and hydrocarbon, CO_2 or radioactive waste. For non-geo-industrial applications, such as monitoring volcanoes, landslides and earthquakes, fractures have a significant influence on the stability of the rock mass and so have important implications on geo-hazard assessment.

The imaging of fractures plays a critical role in terms of reducing the risk of geo-industrial operations as well as hazard assessment of the rock mass due to natural tectonic activities (e.g., volcanoes and

landslides). Seismic imaging of fractures can be used to infer fracture properties, such as density and size. The most common approaches to seismically image fractures are anisotropic velocity model analysis, amplitude versus offset and azimuth (AVOA) analysis and shear-wave splitting (SWS) analysis. Such methods are based on the fundamental concept that the coherent orientation of fractures induces directionality or anisotropy of elastic properties. Anisotropy results from the scale dependence of the wave and fracture interaction (e.g., 2), where a type of coherent scattering leads to fracture induced elastic anisotropy (e.g., 3).

The analysis of the properties of scattered seismic waves is another approach to characterise the heterogeneous structure of the Earth's subsurface on the global, exploration and engineering scales (e.g., 4; 5; 6; 7). Understanding the scattering process in a fractured medium potentially allows for the characterisation of fracture properties. If the fracture size and spacing are substantially small relative to the seismic wavelength, then coherent fractures can lead to the rock appearing as an effective anisotropic medium with a symmetry axis normal to the strike of fractures (e.g., 8; 2). For such scenarios, application of seismic anisotropy methods (e.g., amplitude versus offset and azimuth and shear-wave splitting) can be used to extract fracture properties, such as fracture orientation and density (e.g., 9; 10; 11). If, however, the fracture size and spacing are on the order of the seismic wavelength, then the fractures will lead to observable scatter in the seismic wavefield causing complex reverberation or coda in the seismic signal (6). In the passive seismic monitoring scenario (e.g., geothermal, volcanoes and petroleum settings), where the dominant source frequency can be potentially relatively high and hence the dominant wavelength relatively short with respect to fracture size, scattering could be a significant and observable seismic attribute.

The scattering strength (i.e., the amount of scattering) of a heterogeneous media depends on the relative lengths scales of the elastic heterogeneities and the probing seismic wavefield. The type of scattering depends on the size (or correlation length) of the heterogeneity a compared to the seismic wavelength λ. Rayleigh scattering occurs when $\lambda_S/a > 1$ (λ_S being the dominant wavelength of the incident shear-wave) with the long wavelength approximation (LWA) being the case when $\lambda_S/a >> 1$ (e.g., 12). In the LWA regime, the medium response is quasi-homogeneous and can be represented by an effective elastic medium where the scattering effects are small. In the Rayleigh scattering regime, the Born approximation is sufficient to describe the weak fluctuation of the medium (e.g., 12). The Mie scattering regime occurs when $\lambda_S/d \rightarrow 1$, where scattering is strong and occurs at large angles with respect to the incident wave (e.g., 12). The geometric scattering regime occurs when ($\lambda_S/d < 1$), where focusing/defocussing, diffraction and interference effects are often observed (e.g., 12).

In general there are two approaches to model fractured rock: effective medium models (EMM) and discrete fracture models (DFM). EMM is the most common approach for modelling the seismic behaviour of fractured rock (e.g., 13; 14). EMM is a volumetric approach and models the fractured rock as an effective elastic medium, such that the elastic constants are anisotropic (e.g., 15; 16; 17). There are limitations to EMM, specifically the range of applicable frequencies, the types of fracture properties that can be examined, and the influence non-uniform or non-smooth stress-fields (e.g. 18; 2). The main restriction for EMM is that it is valid only when the dominant seismic wavelength of the propagating wave is much greater than the heterogeneity induced by the fractures; this is referred to as the long wavelength approximation (LWA). Furthermore, EMM assumes the rock mass is 'instantaneously' anisotropic and so does not allow for the transition from a scattering regime to an effective anisotropy regime.

An another approach is to model fractures as discrete surfaces that can characterise individual fracture behaviour (e.g. 18). DFM allows relaxing many assumptions about the model and enables the solution to simulate the interaction of seismic waves with fractures systems more accurately. DFM models can capture the influence of the stress state, as well as specific fracture properties such as fracture size, fill and compliance. Furthermore, DFM is not restricted by the LWA and allows the dominant seismic wavelength to be greater, less than or equal to the fracture

size, allowing the characterisation of low-frequency behaviour (i.e., LWA regime) and high-frequency behaviour (i.e., ray theoretical limit). However, it is generally difficult to determine the spatial geometry of fracture systems deterministically and often the computational costs associated with modelling discrete fractures can be a barrier.

In this study, we use the FD algorithm WAVE (18) because it is capable of modelling fracture networks as individual fractures defined as explicit discontinuity, where distribution of the fracture network can be populated randomly. The aim of this study is to investigate the scattering characteristic of shear-waves as a function of the scale length of the heterogeneity (i.e., fracture size) and is an extension of the anisotropic shear-wave splitting analysis of (2). We present the parameters of the numerical models, and subsequently provide qualitative and quantitative analysis of shear-wave scattering on the modelled synthetic seismograms for different source polarisations and propagation paths relative to the fracture orientation. We attempt to address whether or not analysis of seismic shear-wave scattering can contribute insight into *in situ* fracture properties as an additional seismic attribute to that of shear-wave splitting anisotropy (e.g., 2).

2. Waveform modelling

We simulate microseismic waves using the 3D isotropic FD algorithm WAVE (18). Microseismicity associated with geo-industrial applications stems from failure along pre-existing fracture systems or newly formed fractures and as such we would expect fractures to be present within the volume associated with the induced seismicity. WAVE computes the seismic wavefield on an equally-spaced, staggered orthogonal grid, where the variables stress and velocity are staggered in time. The FD algorithm is second-order accurate in time and fourth-order accurate in space. Fractures are defined using the DFM approach, where each fracture is explicitly defined as a displacement discontinuity and the fracture surfaces have zero thickness. The difference in displacements across the two surfaces is related to the stress across the interface, where the stress and displacement discontinuity across the two surfaces are coupled by the fracture normal and tangential stiffnesses.

We generate a suite of models consisting of a baseline isotropic homogeneous model and several isotropic fracture models. All models have the same background isotropic elasticity with density ρ of 2600 kg/m^3, P-wave velocity V_P of 5700 m/s and S-wave velocity V_S of 3200 m/s ($V_P/V_S = 1.78$). To study the scattering characteristics and sensitivity of various fracture sizes, we vary the fracture fracture size a and fracture normal (K_N) and tangential (K_T) stiffnesses, while keeping the fracture density ϵ and fracture compliance ratio Z_N/Z_T constant. We choose a density of $\epsilon = 0.1$ to represent a moderately fractured medium and a compliance ratio $Z_N/Z_T = 0.33$ to represent water-filled fractures (e.g., 19; 20). Although we focus on varying the fracture size, based on the scaling relation of (21), the fracture size a dictates the allowable range of normal compliance (Z_N) and tangential compliance (Z_T). Table 1 summarises the range of fracture stiffness as a function of fracture size.

Fracture size (m)	K_N (Pa/m)	K_S (Pa/m)
6	6×10^{10}	2×10^{10}
10	3×10^{10}	1×10^{10}
20	3×10^{9}	1×10^{9}
50	3×10^{9}	1×10^{9}

Table 1: Summary of fracture properties for all models having $\epsilon = 0.1$ and $Z_N/Z_T = 0.33$.

For fracture size, a, we consider values of 6, 10, 20 and 50 m for several reasons and constrained by the dominant wavelength ($\lambda_S \approx 18$ m) of the shear-wave. For crustal rock, the size (or height) of fractures ranges on the order of between 0.01 to 10 m (e.g., 1; 22). Thus the lower end values of 6 and 10 m represent typical values observed in the field yet having size that approaches the length scale of the dominant wavelength. Values above 10 m allow us to explore the transition from conditions where EMM would be valid to conditions where EMM for fractures would not be valid.

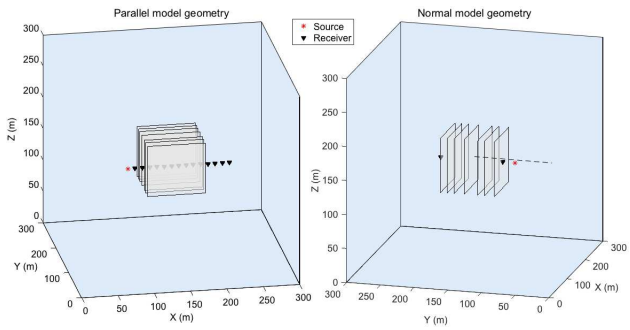

Figure 1: Geometry of 3D FD model. The red star shows the source location, the triangles show the receiver array and the grey rectangles within the sub-volume schematically represent the vertical fractures:(a) the linear receiver array is parallel to the fracture plane and (b) the linear receiver array is normal to the fracture plane. The receiver spacing in the *Parallel* model is 10 m while in the *Normal* model the receiver are 9, 100 and 150 m far from the source. Note that the *Proximal, Exit* and *Distal* stations for both *Parallel* and *Normal* models are 9, 100 and 150 m far from the source.

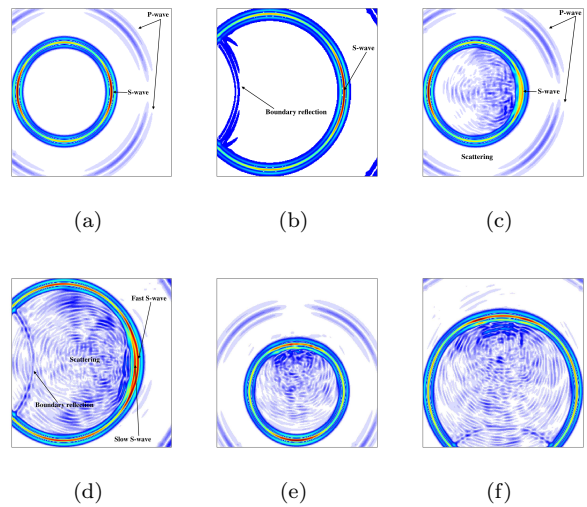

Figure 2: 2D snapshots of seismic wave propagation in the X-Y plane at times 33.1 and 48.9 ms in the isotropic medium (a and b), in the Parallel fracture model (c and d), and Normal fracture model (e and f).

The geometry of all the models have overall dimension of $300 \times 300 \times 300\ m^3$. The fracture models have one set of discrete vertical fractures orientated along the X-axis with fracture volume having dimension of $80 \times 80 \times 80\ m^3$. The fracture models can be divided into two sets that differ in terms of the orientation and number of receivers within the model (see Figure 1). The first fracture model set has a linear array of 15 three-component (3C) receivers placed through the centre of model in the X-direction with receiver spacing 10 m, parallel to fracture strike and referred to as the *Parallel* fracture model. The first receiver is outside the fracture zone in the isotropic background medium on the source side, the subsequent 8 are within the fracture volume and the last 6 are on the outside at the other end. This series of receivers can be used to evaluate the evolution of scattering characteristics when S-waves propagate parallel to the fractured plane (e.g., see 2). The second fracture model set has an array of three 3C receivers placed through the centre of the model in the Y-direction, normal to fracture strike and referred to as the *Normal* fracture model. The first receiver is outside fracture zone in the isotropic background medium on the source side, the second receiver is immediately outside the fracture volume on the opposite side of the source (equivalent to receiver 10 in the parallel model) and the last receiver is on the outside of fracture volume 50 m further than the second receiver (equivalent to receiver 15 in the parallel model). We introduce the *Normal* fracture model to investigate the behaviour of S-waves as they propagate in the normal direction to the fracture planes (the models were extended from 2, where only wave propagation parallel to fracture strike yielded shear-wave splitting). To allow direct comparison between the *Normal* and *Parallel* fracture models, the fracture geometry is kept constant. However, due to the constraints imposed from WAVE implementation, receivers could only be placed outside the fracture zone. Specifically, to generate a fracture volume using the algorithm CRACKGEN (23) the receiver locations are required a priori and thus embedding receivers within the fracture volume would require creating a different fracture volume realisation. Here after, we refer to station 1 as the *Proximal* station, station 2

in *Normal* model and station 10 in *Parallel* model as the *Exit* station and station 3 in the *Normal* model and station 15 in the *Parallel* model as the *Distal* station.

Seismic waves are generated using a moment tensor source having a seismic moment magnitude 1×10^{14} dyne cm and a strike-slip double-couple mechanism with strike of 90°, dip of 90° and slip of 45° for the *Parallel* fracture model and a strike of 0°, dip of 90° and slip of 45° for the *Normal* fracture model. These double-couple source mechanisms allow the source polarisations in the Y-Z and the X-Z planes to be equally partitioned. The source is located at (x_s, y_s, z_s) = (100 m, 150 m, 140 m) for the *Parallel* model and (x_s, y_s, z_s)=(150 m, 200 m, 150 m) for the *Normal* model. For each model, a Ricker source wavelet with a dominant frequency of approximately 180 Hz is used. Thus, based on dispersion and stability requirements, a grid spacing of $dh = 1$ m and time increment of approximately $dt = 0.08$ ms are used. Figure 2 displays snapshots of wave propagation in the X-Y horizontal plane for the isotropic baseline model, *Parallel* fracture model and the *Normal* fracture model at propagation times 33.1 and 48.9 ms. The evolution of the scattered energy is highlighted within the big circle for the fractured models. The splitting of the shear-waves in the *Parallel* model is visible (Figure 2d).

3. Results

We evaluate the scattering characteristics of the fracture models using different quantitative techniques, such as envelope broadening, amplitude spectrum and polarisation analysis. However, before focusing on the quantitative results, we first examine the scattered shear waves from a qualitative perspective to gain insight into the scale dependence of fracture size.

3.1. Qualitative analysis of shear-wave coda

Figure 3 shows the 3C seismograms from the *Parallel* fracture models for all fracture sizes. Although the MT source prescribes initial polarisations of equal magnitude on the Y- and Z-components for the *Parallel* models, small forward scattered energy can be observed on the X-component due to edge and tip diffractions. As expected, the Y- and Z-components are initially equal at the *Proximal* station, but with increasing distance from the source there are significant changes in the waveforms, especially for $a = 20$ m, where $\lambda_S \approx 18$ m. We observe a transition from the long wave approximation (LWA) or Rayleigh scattering (where $\lambda_S/a > 1$) for $a = 6$ and 10 m to the Mie scattering regime (where $\lambda_S/a \to 1$) for $a = 20$ m. For fracture size a=50m, the scattering regime falls under the geometric regime.

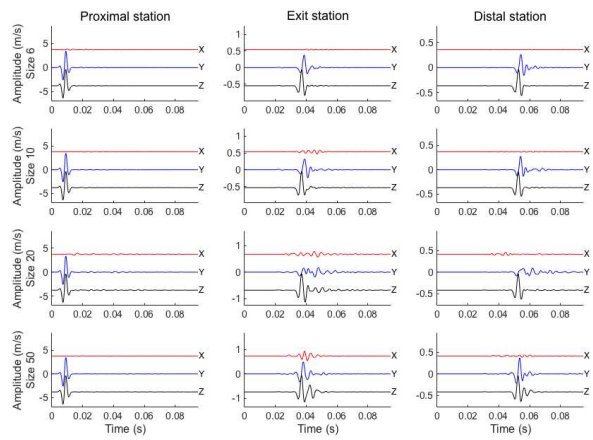

Figure 3: Three-component waveforms observed at the *Proximal, Exit* and *Distal* stations in the *Parallel* model with fractures size 6, 10, 20 and 50 m. Hereafter the components are depicted: X-component (red color), Y-component (blue) and Z-component (black).The arrows for the station 6 show the P- and S-wave signals. Amplitude is particle velocity in mm/s.

Figure 4 displays the 3C seismograms for the *Normal* fracture models for all desired fracture sizes a = 6 m, 10 m, 20 m and 50 m. For the *Normal* model, the MT source prescribes initial polarisations of equal magnitude on the X- and Z-components. As in the case for the *Parallel* model, small forward scattered energy can be observed on the Y-component due to edge and tip diffractions. For the *Proximal* station, as the fracture size increases from 6 m to 50 m, we observe an increase in signals arriving after the primary wave. These signals are related to increasing specular reflections from the fracture zone as the fracture surface becomes larger with respect to the dom-

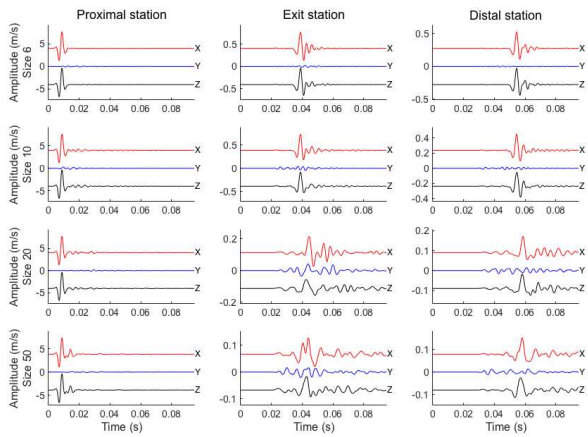

Figure 4: Three-component waveforms observed at the *Proximal, Exit* and *Distal* stations in the *Normal* models with fracture size 6, 10, 20 and 50 m.

inant seismic wavelength. For the *Exit* station, we observe a substantial amount of scattering, specifically when the fracture size is comparable or larger than the wavelength of the S-wave ($\lambda_S \approx 18$ m) at $a = 20$ m and 50 m.

3.2. RMS envelope analysis

To evaluate the time widening effect of wavelets due to scattering within the fractured medium, we compute the root-mean-square (RMS) waveform envelopes. The envelope width approach has been used previously to characterise random heterogeneities in the crust by (24), where the width can be qualify by the parameter t_q and depends on the intensity of velocity fluctuation, scale length of the random heterogeneity as well as attenuation factor Q^{-1}. The RMS envelope is estimated using the following steps:

1. Calculate the square amplitude of the waveform,
2. Average the square amplitude trace using a moving time window (we use a time window of length 7.9 ms which is approximately greater than the width of the source envelope),
3. Calculate the square root of step (2), and
4. Smooth the result in step (3).

The strength of excitation of the scattered waves can be quantified by measuring the envelope width t_q. The envelope t_q is defined by the interval time from the onset of the shear wave to the time when the RMS envelope amplitude decreases to the half of its maximum value.

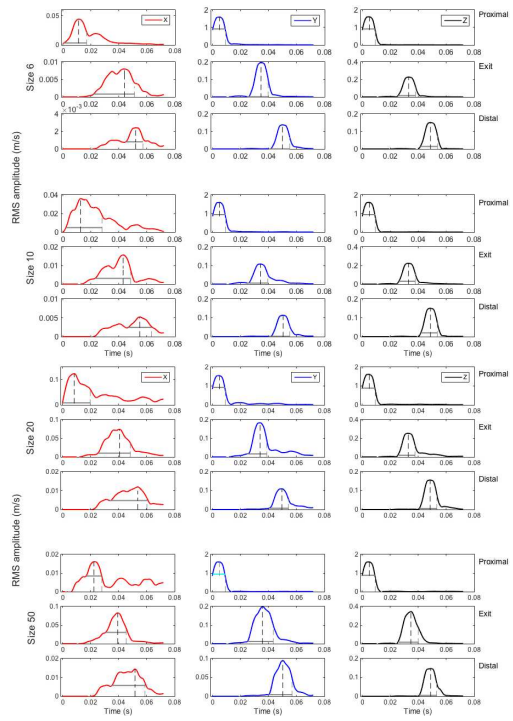

Figure 5: Three-component RMS envelopes observed at the *Proximal, Exit* and *Distal* stations in the fractured medium (*Parallel*) with fracture size 6, 10, 20 and 50 m. The black dashed line shows the maximum RMS envelope, and thick grey line depicts the envelope width time t_q.

Figure 5 shows the three 3C RMS envelopes of the *Parallel* fracture model for all fracture sizes. As expected, the RMS amplitude of the X-component is smaller by one order of magnitude than the Y- and Z-components. As the shear-wave propagates through the fracture volume we observe a gradual decrease in the amplitude of the envelopes with minor changes in the shape of the envelope for the Y- and Z-components and more drastic changes for the X-component. Figure 6 shows the three 3C RMS envelopes for *Normal* fracture models for all fracture sizes. Similar to Figure 5, the components

normal to wave propagation (X- and Z-components) have approximately the same initial RMS amplitude, whereas the component along the direction of propagation (the Y-component) displays initial RMS amplitude one order of magnitude smaller than the X- and Z-components as well as drastically different envelope shapes. The RMS envelopes for the X- and Z-components show significant change for fracture sizes $a = 20$ and 50 m.

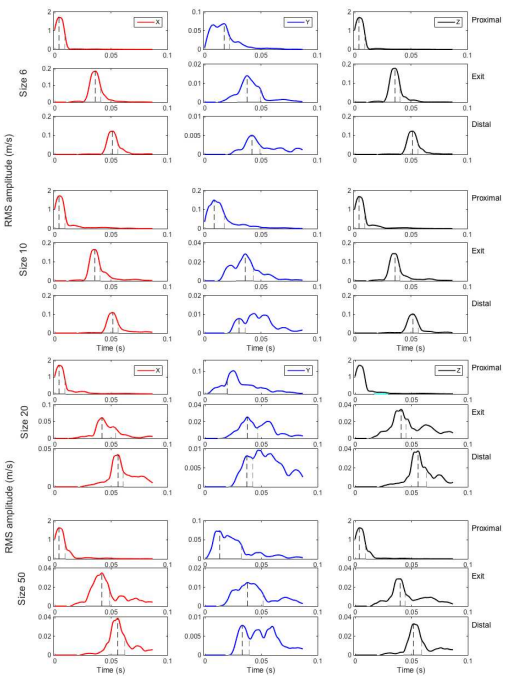

Figure 6: Three-component RMS envelopes observed at the *Proximal, Exit* and *Distal* stations in the fractured medium (*Normal*) with fracture size 6, 10, 20 and 50 m. The black dashed line shows the maximum RMS envelope, and thick grey line depicts the envelope width time t_q.

To remove the effect of geometrical spreading, the t_q values for each station in the *Parallel* and *Normal* models are divided by the t_q values of the corresponding isotropic homogeneous baseline model. As the effective seismic moment tensor source radiation pattern is equivalent in the *Parallel* and *Normal* models, the results of the $\overline{t_q}$ values for the three primary axes of polarisation, X-, Y-, and Z-axes are comparable. In Figure 7, the $\overline{t_q}$ results for the X- and Z-components from the *Normal* model and the Y- and Z-components from the *Parallel* model are shown together. For the *Proximal* station in both the *Parallel* and *Normal* models, the $\overline{t_q}$ values are approximately 1.0 as would be expected of the wavefield prior to entering the fracture zone (i.e., no scattering). Also shown are the values for the *Exit* and *Distal* stations, which show the results of the wave after exiting the fracture volume. At the *Exit* station, the $\overline{t_q}$ values increase above 1.0, with a more significant increase for $a > 10$ m. The $\overline{t_q}$ values between $a = 20$ to 50 m decrease for the *Normal* model at the *Distal* station in comparison with those at the *Exit* station with the exception of the Z-component. In general, the $\overline{t_q}$ values for the *Normal* model, with propagation direction normal to the fracture plane, are larger than those for the *Parallel* model. This can be explained by the fact that for propagation in the direction normal to the fractures the wavefront interacts to a much larger extent with the fracture surfaces and so experiences much greater edge and tip diffractions than for wave propagation parallel to the fractures.

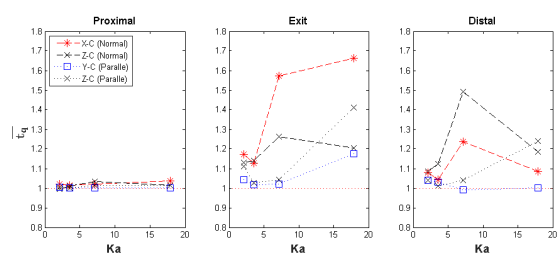

Figure 7: Plot of the normalised envelope width $\overline{t_q}$ against ka for the fracture sizes 6, 10, 20 and 50 m for both the *Parallel* and *Normal* models.

3.3. Distortion of shear-wave polarisation

In a homogeneous isotropic medium, the particle motion of the P-wave is normal to the spherical wavefront and the polarisation of the S-wave is confined to within the wavefront (i.e., normal to the propagation direction) and prescribed by the source radiation pattern. However, in a heterogeneous medium, P-wave particle motion and S-wave polarisation can

deviate from linearity. The deviation from linearity (or waveform distortion) can be assessed by tracking the trajectory of the waveform particle motion. The shape of the time evolution of the particle motion (or hodogram) can be diagnostic of the seismic waveform distortion. A number of earlier studies have shown the usefulness of hodograms for detecting heterogeneity (e.g., 25; 26; 27).

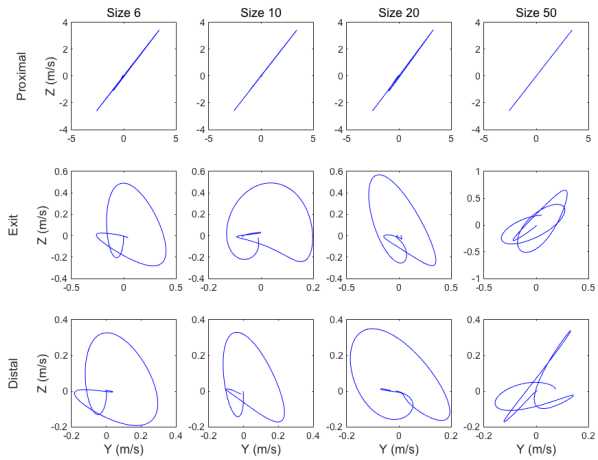

Figure 8: Particle motion of S-waves in the Y-Z plane for the *Parallel* model with fracture sizes 6, 10, 20 and 50 m. Here and in Figure 9, the time window is set from the onset of the S-wave and has a time length two times the period of the Ricker source wavelet.

Figure 8 displays the particle motion of the direct S-waves in the Y-Z plane for the *Parallel* model for all fracture sizes at the 3 stations. The *Proximal* station shows a linear particle motion as expected for wave propagation in a homogeneous isotropic medium. With increasing distance from the source, the waveforms become increasingly distorted and deviate from linear motion. For fracture sizes a= 6 and 10 m, the particle motion of the S-wave components display a characteristic pattern typical of shear-wave splitting with orthogonal fast and slow shear-waves (e.g., see 2). For fracture sizes a= 20 and 50 m, the polarisation is not consistent with that of shear-wave splitting and shows a more random behaviour.

Figure 9 displays the particle motion for the *Normal* model for all fracture sizes at the 3 stations. For

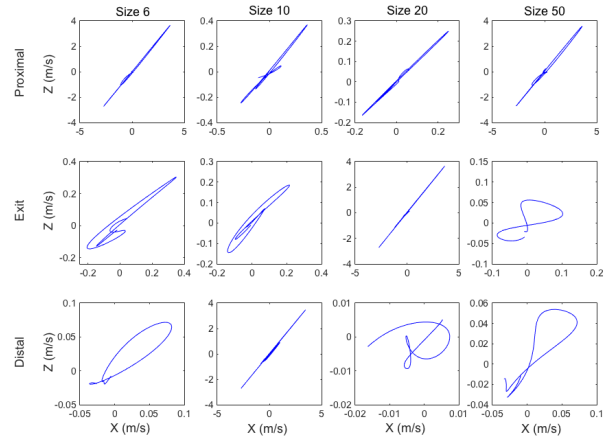

Figure 9: Particle motion of S-waves in the X-Z plane for the *Normal* model with fracture sizes 6, 10, 20 and 50 m.

all fracture sizes at the *Proximal* station, the particle motions are linear as expected. At the *Exit* and *Distal* stations, with increasing fracture size the distortion from linearity also increases. For wave propagation normal to the fracture planes shear-wave splitting will not develop. Although the waveform envelopes have been shown to increase, the actual polarisation of the shear-waves remain relatively unaffected for scenarios where $ka \leqslant 3$. For $ka > 3$, we observe significant deviation from linearity, primarily as a result of the multiple reverberations due to specular type reflections from the interaction of the spherical wavefront and the fracture surfaces (i.e., stronger coherent scattering).

To quantitatively evaluate the distortion of the direct shear-waves, the RMS amplitude ratio between the Y- and Z-components for *Parallel* models, and the X- and Z-components for *Normal* models are calculated. The RMS amplitude ratios are calculated according to

$$\chi_{Parallel} = \sqrt{\frac{\sum_i RMS_{z_i}}{\sum_i RMS_{y_i}}}, \tag{1}$$

$$\chi_{Normal} = \sqrt{\frac{\sum_i RMS_{z_i}}{\sum_i RMS_{x_i}}}, \tag{2}$$

where RMS_{x_i}, RMS_{y_i} and RMS_{z_i} are the RMS amplitudes of X, Y and Z components at time t_i, respectively. The summation is evaluated over a time window that is two times the dominant period (11 ms) of the S-wave source from the onset.

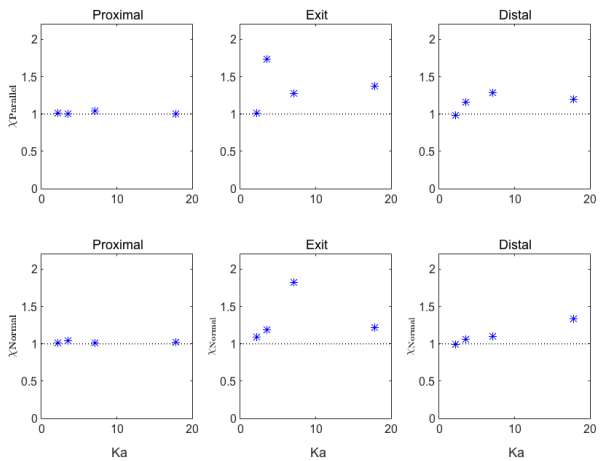

Figure 10: Plot of the RMS ratio $\chi_{Parallel}$ (top) and χ_{Normal} (bottom) against ka for the fracture sizes 6 m (ka=2.1), 10 m (ka=3.6), 20 m (ka=7.2) and 50 m (ka=17.9).

Figure 10 shows the RMS amplitude ratio for $\chi_{Parallel}$ and χ_{Normal} against ka for all fracture sizes. For a = 6 m and all stations the values of $\chi_{Parallel}$ and χ_{Normal} are very close to 1.0, which indicates that the same amount of the energy is partitioned into the Y- and Z-components and X- and Z-components for the *Parallel* and *Normal* fracture models, respectively. For fracture sizes a = 10, 20 and 50 m, the values of $\chi_{Parallel}$ are noticeably larger than 1.0. For the *Exit* station, the $\chi_{Parallel}$ value is highest for a=10 m at approximately 1.75 and roughly 1.25 for a > 10 m. For the *Exit* station, the χ_{Normal} value is highest for a= 20 m at approximately 1.8 and roughly 1.2 for a= 10 and 50 m. At the *Distal* stations, the $\chi_{Parallel}$ and χ_{Normal} values appear more stable and fluctuate between 1.1 and 1.4 for both the *Parallel* and *Normal* models. It can seen that the largest distortion occurs when the fracture size a is comparable to or larger than the dominant wavelength λ_S (i.e., a =20 m) in the Mie and geometric scattering regime. Since the fracture models used in WAVE are generated using random fracture assemblies given a range of fracture size and fracture density (18), the results from *Exit* station represent behaviour of the wavefield highly dependent on the specific random realisation of the fracture model. Thus the results capture the wavefield prior to wavefront healing (e.g., 28). It would be expected that an ensemble of several hundred fracture realisations would yield behaviour consistent with the *Distal* station.

3.4. Differential attenuation analysis

There are several techniques to measure wave attenuation, such as the centroid frequency shift method (e.g., 29), the dominant frequency shift method (e.g., 30) and the spectral ratio method (e.g., 31). We first consider the waveform frequency content of both the *Parallel* and *Normal* models and then discuss and implement the spectral analysis method to quantify attenuation.

3.4.1. Amplitude spectrum analysis

A Hanning window has been used to taper the shear-waves prior to Fourier transformation into the frequency domain. The window length varies depending on the model fracture size. As well, the effect of geometrical spreading is eliminated for each component by normalising the amplitude spectrum by its corresponding station component in the unfractured isotropic medium. We compute the peak (maximum) frequency as well as the dominant frequency at each station and for each component. The dominant frequency is given (30)

$$f_d^2 = \frac{\int_0^\infty f^4 P(f) df}{\int_0^\infty f^2 P(f) df}, \tag{3}$$

where f_d is the dominant frequency and $P(f)$ is the power spectrum.

Figure 11 shows the amplitude spectrum for the *Parallel* models for all fracture sizes for the Z- and Y-components. For all fracture sizes, the amplitude spectrum of the Y-component is more attenuated at higher frequencies than Z-component. This is expected as the Y-component is polarised normal to

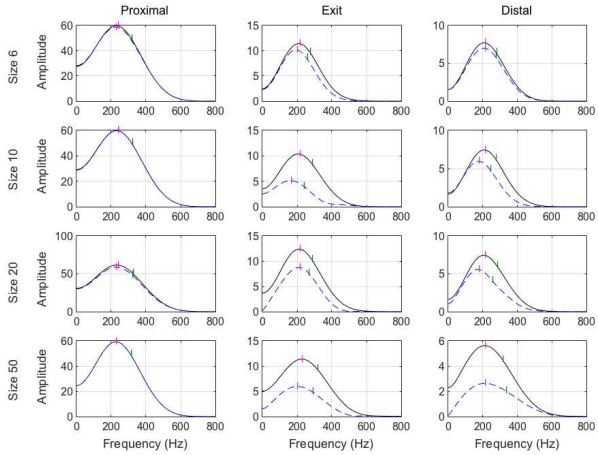

Figure 11: Fourier amplitude spectrum for all fracture sizes for the *Parallel* model. The solid black line depicts the Z-component, the blue dashed line depicts the Y-components, and the small green and magenta bars, respectively show the dominant and peak frequencies of spectra.

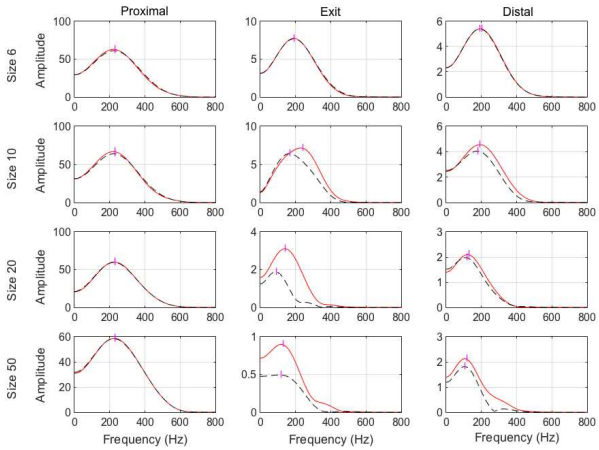

Figure 12: Fourier amplitude spectrum for all fracture sizes for the *Normal* model. The solid red line depicts the X-component and the black dashed line depicts the Z-components.

the fracture surface whereas the Z-component is polarised parallel to the fracture surface. Figure 12 shows the amplitude spectra for the *Normal* models at the 3 stations for all fracture sizes. With the exception of the *Proximal* station (where the spectra results are very closely equal) the remaining stations reveal that the Z-component is more attenuated at higher frequencies than the X-component. For both components, the peak frequencies have shifted to lower frequencies; the shift being greatest for models with larger fracture size.

3.4.2. Amplitude spectral ratio

Since fractures form within coherent and subparallel patterns, seismic velocity will be dependent on the direction of wave propagation. For instance, P-waves propagating parallel to the fracture planes will travel faster than P-waves propagating normal to the fracture planes. The velocity between these two directions depends on several variables, such as the medium elastic constants, pore-fluid properties and saturation, the fracture density as well as the distribution and shape of fractures (e.g., 32). The presence of aligned fracture sets often results in seismic anisotropy, although there is a transition where a fractured medium evolves from a scattering to anisotropic regime (e.g., 2). Velocity anisotropy is theoretically formulated for various types of anisotropic symmetries, such as transverse isotropy (TI), azimuthal anisotropy and fracture-induced anisotropy. Yet, velocity anisotropy alone is not sufficient to reveal the reasons that lead to elastic anisotropy. For instance, crystal scale lattice preferred orientation (LPO) and aligned fractures can theoretically result in the same observed anisotropy. However, attenuation anisotropy can differ between these two causes of observed anisotropy and this is due to frequency-dependent mechanisms (e.g., 33; 34). For instance, when the scale length of heterogeneity is smaller than the seismic wavelength, low frequency waves will accrue longer splitting times than high frequency waves (e.g., 32). For media where the wave velocity is frequency-dependent, the medium elasticity is required to be dispersive.

There is a relation between dispersion and intrinsic attenuation (e.g., 35; 36). (36) studied velocity and attenuation anisotropy of vertically fractured media with low fracture density and introduced a model valid in the high frequency limit, where wavelengths are larger than fracture size. The (36) model predicts

that the slow shear-wave will be more attenuated at higher frequencies relative to the fast shear-wave. (33) extended the (36) model and showed the dependency of shear-wave splitting on waveform frequency and fracture size. (32) tested the (36) model on several microseismic datasets of shear-waves splitting to predict attenuation of the split shear-waves. However, (32) observed that sometimes the fast shear-wave was more attenuated at higher frequencies than the slow shear-wave.

To study the differential shear wave attenuation, we implement the spectral ratio method for the Y- and Z-components for the *Parallel* models and the X- and Z-components for the *Normal* models. To do this, the intrinsic attenuation Q^{-1} is assumed to be a constant. For our models, this assumption is adequate since the background elasticity is non-attenuative. For the *Parallel* models, where the propagation direction is along the strike of the fracture planes and for the initial prescribed source polarisation orientation, shear-wave splitting has the potential to develop in the synthetic data. Hence, the calculation of differential attenuation ΔQ^{-1}_{Z-Y} for the *Parallel* models might provide a measure of shear-wave scattering attenuation. Differential attenuation is the difference in the loss of energy per cycle experienced by pairs shear-components along the fractured part of the ray path. The measurement of the quality factor is not a true value, rather it approximates Q^{-1}, and is referred to as specific attenuation.

The amplitude of the shear-wave can be written as a function of frequency f,

$$A_n(f) = G_n(f)S_n(f)R_n(f)exp(\frac{-\pi t_n f}{Q_n}), \quad (4)$$

where $A_n(f)$ is the amplitude spectrum at a particular station, n is the component (i.e., X, Y or Z), $G_n(f)$ is the transfer function between source and station, $S_n(f)$ is the amplitude at the source, $R_n(f)$ is the effective transfer function of the receiver (i.e., including rotation, the coupling, the impulse response of the receiver and the recording system response) and t is the traveltime between source and receiver.

Assuming the pairs of shear-wave components have the same transfer function, the same effective transfer function and the same spectral frequency at the source, then the spectral ratio method (31) can provide a measure of the relative attenuation between two orthogonal components. The calculation of the log amplitude spectral ratio (LASR) for the *Parallel* and *Normal* models, respectively, are formed,

$$ln\left(\frac{A_Z(f)}{A_Y(f)}\right) = -\pi\left(\frac{t_Z}{Q_Z} - \frac{t_Y}{Q_Y}\right)f + c. \quad (5)$$

$$ln\left(\frac{A_Z(f)}{A_X(f)}\right) = -\pi\left(\frac{t_Z}{Q_Z} - \frac{t_X}{Q_X}\right)f + c. \quad (6)$$

(31). The c term is a constant value that results from the frequency-independent differences in the G_n, S_n and R_n values in Equation 4. The t_n values for the *Parallel* and the *Normal* model represent the arrival time for each component. For the *Parallel* model $t_Z \leqslant t_Y$ ($t_Z = t_Y$ if no shear-wave splitting and $t_Z < t_Y$ if there is shear-wave splitting, where the Z-component is the fast shear-wave). For the *Normal* model the $t_Z = t_X$. If attenuation Q is constant, the LASR should be approximately linear with frequency over the signal bandwith. Regression is performed over a limited bandwidth (black dashed line). The differential attenuation for the *Parallel* and *Normal* models, respectively, can be defined as

$$\Delta Q^{-1}_{Z-Y} = \pi t_Z\left(\frac{t_Y}{t_Z Q_Y} - \frac{1}{Q_Z}\right) \quad (7)$$

$$\Delta Q^{-1}_{Z-X} = \pi t_Z\left(\frac{t_X}{t_Z Q_X} - \frac{1}{Q_Z}\right). \quad (8)$$

The term πt_Z is positive, so the remaining term can be either positive or negative. If equation 7 is negative, the Z-component is more attenuated than the Y-component since t_Y/t_Z is greater than or equal to one. However, when Equation 7 is positive, we can not strictly say which component has been more attenuated. Without a measurement of either Q_Z^{-1} or Q_Y^{-1}, it is not possible to know which component has experienced more attenuation at high frequencies due

to the trade-off between the additional travel time of the slow shear-wave spent in the attenuative medium and the magnitude of attenuation affecting the slow component being larger than the fast component (i.e., the slow shear-wave has experienced a greater attenuation per cycle).

Previously, we showd that the Y-component (slow shear-wave) experiences larger attenuation than the Z-component (fast shear-wave), which is consistent with results of (36). However, (32) observe that the fast shear-wave can experience larger attenuation than the slow shear-wave, and suggest that the relative peak amplitude of the split shear-waves are depend more on the initial polarization of the incident shear-wave than on the relative levels of frequency-dependent attenuation.

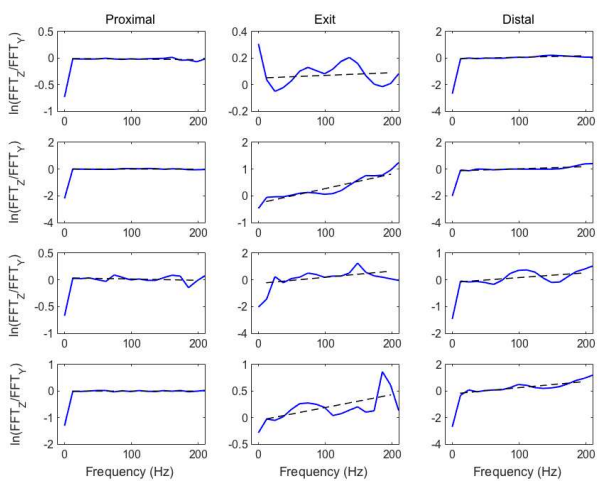

Figure 13: Amplitude spectral ratio of Y- and Z-axis $Log_e(A_Z(f)/A_Y(f))$ of *Parallel* for fracture sizes 6, 10, 20, and 50 m. Here and in Figure 14 the dashed line shows the regression line over limited bandwidth.

Figure 13 shows the LASR for *Parallel* models for all fracture sizes. The regression lines (black dashed lines) reveal a positive gradient over the bandwidth of 0-200 Hz. The positive gradient suggests that the Y-component is more attenuated than the Z-component. The difference between peak frequency of the shear-waves is positive ($f_{p_Z} - f_{p_Y} > 0$) also indicating that the Y-component is more attenuated. However, it is not possible to determine whether $Q_Z > Q_Y$ or whether $Q_Z \approx Q_Y$ sine the Y-component could be more attenuated due to the longer travel time in the fractured medium.

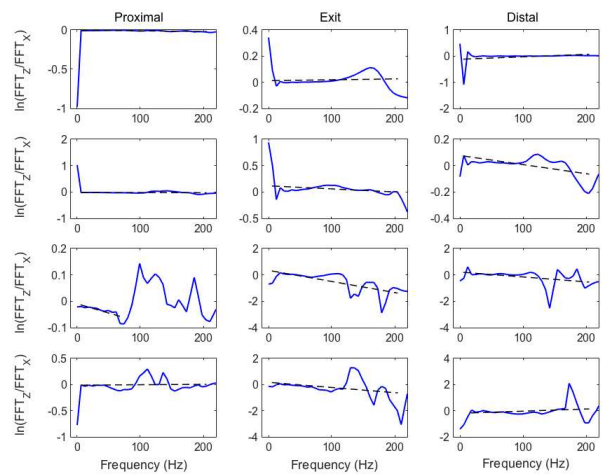

Figure 14: Amplitude spectral ratio of Y- and Z-axis $Log_e(A_Z(f)/A_Y(f))$ of *Normal* for fracture sizes 6, 10, 20, and 50 m.

The LASR for the *Normal* model can be simplified based on the assumption that the shear-wave onset times will be equal ($t_X = t_Z$)

$$\Delta Q^{-1}_{Z-X} = \pi t_Z \left(\frac{1}{Q_X} - \frac{1}{Q_Z} \right). \tag{9}$$

The term πt_Z is positive and the remaining term in brackets can be either positive or negative. If Equation 9 is positive, the X-component is more attenuated than Z-component ($Q_X^{-1} > Q_Z^{-1}$). Equation 9 intuitively reveals that differences in attenuation between the X- and Z-components in the *Normal* model are not influenced by differential travel times. The LASR for the Z- and X-components of the *Normal* model is shown in Figure 14, where the regression gradient lines (black dashed line) for almost all the stations is negative. The negative regression line implies that $Q_Z^{-1} > Q_X^{-1}$. However, with the exception of a few frequency notches, the slopes are approximately horizontal. We would expect that the X- and

Z-component attenuation to be identical and so the results are likely influenced by focusing and defocusing of discrete frequency bands due to the specific random realisation of the fracture volume. Combining the results from several hundred random fracture realisations would likely yield equal attenuation of both components.

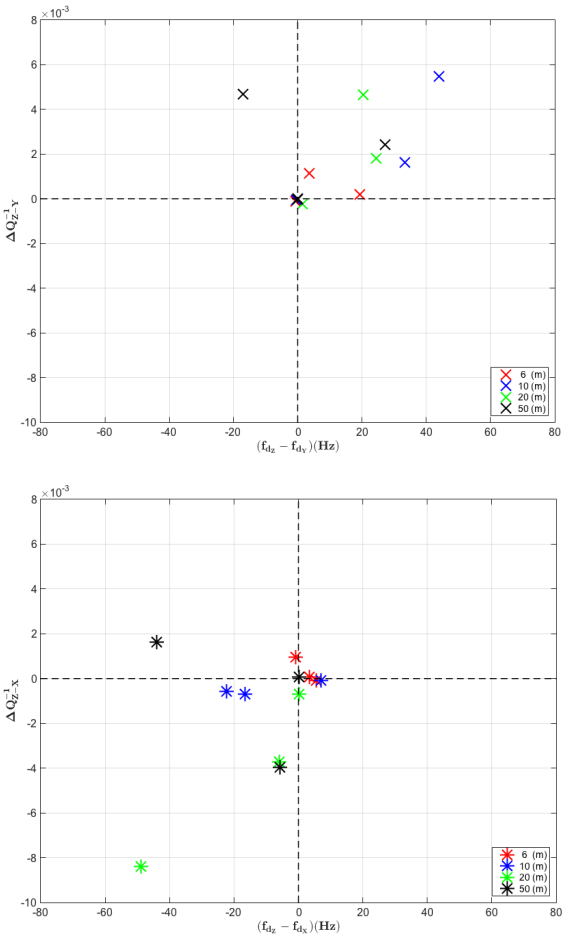

Figure 15: Differential attenuation plotted against difference in peak frequency, $f_{p_Z} - f_{p_Y}$ for the *Parallel* (a) model and $f_{p_Z} - f_{p_X}$ for the *Normal* model (b).

Figure 15 depicts the differential attenuations (ΔQ^{-1}_{Z-Y} and $f_{p_Z} - f_{p_Y}$) against the difference in the peak frequencies $f_{p_Z} - f_{p_Y}$ and the dominant frequency $f_{d_Z} - f_{d_Y}$ respectively. It can be seen that the differential attenuation in the *Parallel* model $\Delta Q^{-1}_{Z-Y} > 0$ is consistent with the observation of a shift in the peak frequency $f_{p_Z} - f_{p_Y} \geqslant 0$. However, it can be seen that for the *Normal* model the differential attenuation $\Delta Q^{-1}_{Z-X} < 0$, while $f_{p_Z} - f_{p_X} \leqslant 0$. These results imply that the differential attenuation method is adequate to examine the attenuation of each component individually, except when $\Delta Q^{-1}_{Z-Y} > 0$. In addition, differential attenuation is an appropriate method and is compatible with method of peak frequency shift.

4. Discussion

The results of the shear-wave scattering analysis suggest that there are qualitative and quantitative differences in scattering behaviour for the various fracture sizes. Very little scattering is observed for fracture size $a = 6$ m within the Rayleigh scattering regime. (2) observe that shear-wave anisotropy is strongest and more coherent in the Rayleigh regime, such that seismic anisotropy is an appropriate technique to characterise fracture properties with this regime. The most noticeable scattering effects are observed for fracture sizes $a = 20$ and 50 m, within the Mie scattering and transition to geometrical scattering regime. The quantitative measures all indicate strong deviation from the background for both propagation parallel and normal to the fracture surfaces. However, for the *Parallel* model the largest $\overline{t_q}$ (envelope width) was obtained for the largest fracture size ($a = 50$ m), while for the *Normal* model the largest $\overline{t_q}$ occurred for fracture size, $a = 20$ m (where a is approximately equal to the λ_S). (37) and (38) theoretically examined the scattering characteristics of shear-waves of planar cracks of finite width for $ka \geqslant 3$. Based on their results, scattering is prominent when the shear-wave propagates perpendicular to the fracture planes. In general, the average $\overline{t_q}$ values for the *Normal* model were generally larger than the *Parallel* model. This is consistent with theory and is likely due to the wavefront interactions with fracture surfaces that result in diffraction from fracture tips and edges.

Previous studies have shown that cracks introduce a frequency dependent elastic response (e.g.,

39; 40; 3; 41; 14), where the frequency dependence is explained by squirt-flow mechanisms due to wave-induced fluid flow in fractured porous rocks (e.g., 33) and/or scattering mechanisms due to wave propagation through rough fracture surfaces having heterogeneous stiffness distributions (e.g., 39; 18). In this study, we have only focused on the scale-dependence of shear-wave scattering and notice very little frequency dependence with the exception of a general attenuation of higher frequencies as the shear-wave propagates through a fracture volume. Although the results from this chapter remain inconclusive in terms of using shear-wave scattering phenomena as means of imaging fracture properties, such as fracture size, previous works suggest that considering the frequency-dependent response can provide constraint of fracture size and fracture infill (e.g., 33; 34; 14). However, it should be noted that in real passive seismic data, there will be a range of seismic source sizes depending on the strength of the stress redistribution as well as the length scales of the internal material weaknesses. In theory, low-magnitude microseismic events typically have a higher dominant frequency than larger magnitude events and this relates to the size of the rupture surface initiated by failure. As such, passive seismic data will contain a wide range of illumination sources displaying differing scale-dependent interaction with the *in situ* fractures.

5. Conclusion

We examined the widening effect of wavelets due to scattering within a fractured medium by using several different approaches. The examination was performed by implementing numerical modelling of wave propagation in discrete fracture models with a desired fracture density and for various fracture sizes. We used different methods including the RMS envelope analysis, shear-wave polarisation distortion, differential attenuation analysis and peak frequency shifting to assess the scattering behaviour of those parametrised models in which the propagation direction is either normal or parallel to the fracture surfaces. The quantitative measures show strong observable deviations for fractures size on the order of or greater than the dominant seismic wavelength within the Mie and geometric scattering regime for both propagation normal and parallel to fracture strike. The results suggest that strong scattering is symptomatic of fractures having size on the same order of the probing seismic wave.

Acknowledgements

The authors would like to thank Mark Hildyard for providing assistance in using the finite-difference algorithm WAVE and the fracture model builder CRACKGEN. D. Angus acknowledges the Research Council UK (EP/K035878/1; EP/K021869/1; NE/L000423/1) for financial support.

References

References

[1] W. Narr, D. W. Schechter, L. B. Thompson, Naturally fractured reservoir characterization, Society of Petroleum Engineers, Richardson, TX, 2006.

[2] B. M. Yousef, D. A. Angus, When do fractured media become seismically anisotropic? some implications on quantifying fracture properties, Earth and Planetary Science Letters 444 (2016) 150–159.

[3] E. Liu, A. Martinez, Seismic fracture characterization: Concepts and practical applications (2012) 280.

[4] F. Shen, M. N. Toksöz, Scattering characteristics in heterogeneously fractured reservoirs from waveform estimation, Geophysical Journal International 140 (2) (2000) 251–266.

[5] P. M. Shearer, P. S. Earle, The global short-period wavefield modelled with a monte carlo seismic phonon method, Geophysical Journal International 158 (3) (2004) 1103–1117.

[6] M. E. Willis, D. R. Burns, R. Rao, B. Minsley, M. N. Toksöz, L. Vetri, Spatial orientation and distribution of reservoir fractures from scattered seismic energy, Geophysics 71 (5) (2006) O43–O51.

[7] L. Margerin, Seismic waves, scattering, in: H. Gupta (Ed.), Encyclopedia of Solid Earth Geophysics, Springer, 2011.

[8] E. R. Liu, J. A. Hudson, T. Pointer, Equivalent medium representation of fractured rock, Journal of Geophysical Research-Solid Earth 105 (B2) (2000) 2981–3000.

[9] M. Willis, F. Pearce, D. Burns, J. Byun, B. Minsley, Reservoir fracture orientation and density from reflected and scattered seismic energy, in: 66th EAGE Conference & Exhibition, 2004.

[10] Y. Zhang, S. Chi, M. E. Willis, D. Burns, T. M. Nafi, Comparison of discrete fracture and effective media representation of fractures on azimuthal avo, 75th Annual Meeting of the Society of Exploration Geophysicists (SEG 2006).

[11] Y. Zhang, S. Chi, M. E. Willis, M. N. Toksoz, D. R. Burns, Orientation estimation for multiple large fractures by scattering energy, Report, Massachusetts Institute of Technology. Earth Resources Laboratory (2006).

[12] H. Sato, M. C. Fehler, Seismic Wave Propagation and Scattering in the Heterogeneous Earth, Springer, 1998.

[13] S. A. Hall, J.-M. Kendall, Constraining the interpretation of avoa for fracture characterisation, Anisotropy 2000: Fractures, converted waves, and case studies (2000) 107–144.

[14] A. F. Baird, J.-M. Kendall, D. A. Angus, Frequency-dependent seismic anisotropy due to fractures: Fluid flow versus scattering, Geophysics 78 (2) (2013) WA111–WA122.

[15] R. J. O'Connell, B. Budiansky, Seismic velocities in dry and saturated cracked solids, Journal of Geophysical Research 79 (35) (1974) 5412–5426.

[16] S. Crampin, A review of wave motion in anisotropic and cracked elastic-media, Wave motion 3 (4) (1981) 343–391.

[17] C. Sayers, M. Kachanov, A simple technique for finding effective elastic constants of cracked solids for arbitrary crack orientation statistics, International Journal of Solids and Structures 27 (6) (1991) 671–680.

[18] M. Hildyard, Manuel rocha medal recipient wave interaction with underground openings in fractured rock, Rock Mechanics and Rock Engineering 40 (6) (2007) 531–561.

[19] R. Lubbe, J. Sothcott, M. H. Worthington, C. McCann, Laboratory estimates of normal and shear fracture compliance, Geophysical Prospecting 56 (2) (2008) 239–247.

[20] J. P. Verdon, A. Wüstefeld, Measurement of the normal/tangential fracture compliance ratio (zn/zt) during hydraulic fracture stimulation using s-wave splitting data, Geophysical Prospecting 61 (s1) (2013) 461–475.

[21] M. Worthington, R. Lubbe, (), Geological Society, London, Special Publications 270 (1) (2007) 73–82.

[22] N. Barton, Rock quality, seismic velocity, attenuation and anisotropy, CRC press, 2007.

[23] M. W. Hildyard, Wave interaction with underground openings in fractured rock, Thesis (2001).

[24] H. Sato, Broadening of seismogram envelopes in the randomly inhomogeneous lithosphere based on the parabolic approximation: Southeastern honshu, japan, J. geophys. Res 94 (B12) (1989) 17735–7747.

[25] O. Nishizawa, C. Pearson, J. Albright, Properties of seismic wave scattering around water injection well at fenton hill hot dry rock geothermal site, Geophysical Research Letters 10 (1) (1983) 101–104.

[26] T. Nishimura, Horizontal layered structure with heterogeneity beneath continents and island arcs from particle orbits of long-period p waves, Geophysical Journal International 127 (3) (1996) 773–782.

[27] Y. Fukushima, O. Nishizawa, H. Sato, M. Ohtake, Laboratory study on scattering characteristics of shear waves in rock samples, Bulletin of the seismological Society of America 93 (1) (2003) 253–263.

[28] T. M. Müller, S. A. Shapiro, Most probable seismic pulses in single realizations of two-and three-dimensional random media, Geophysical Journal International 144 (1) (2001) 83–95.

[29] Y. Quan, J. M. Harris, Seismic attenuation tomography using the frequency shift method, Geophysics 62 (3) (1997) 895–905.

[30] A. E. Barnes, Instantaneous spectral bandwidth and dominant frequency with applications to seismic reflection data, Geophysics 58 (3) (1993) 419–428.

[31] B. Båth, Spectral analysis in geophysics, Elsevier, Amsterdam, 1974.

[32] A. J. Carter, J. M. Kendall, Attenuation anisotropy and the relative frequency content of split shear waves, Geophysical Journal International 165 (3) (2006) 865–874.

[33] M. Chapman, S. Maultzsch, E. Liu, X.-Y. Li, The effect of fluid saturation in an anisotropic multi-scale equant porosity model, Journal of Applied Geophysics 54 (3) (2003) 191–202.

[34] S. Maultzsch, Analysis of frequency-dependent anisotropy in vsp data, Ph.D. thesis, University of Edinburgh (2005).

[35] K. Aki, P. Richards, Quantitative seismology, Vol. 1424, Freeman San Francisco, 1980.

[36] J. A. Hudson, Wave speeds and attenuation of elastic-waves in material containing cracks, Geophysical Journal of the Royal Astronomical Society 64 (1) (1981) 133–150.

[37] F. Neerhoff, J. Van der Hijden, Diffraction of elastic waves by a sub-surface crack (anti-plane motion), Journal of Sound and Vibration 93 (4) (1984) 523–536.

[38] J. Van Der Hijden, F. Neerhoff, Scattering of elastic waves by a plane crack of finite width, Journal of Applied Mechanics 51 (3) (1984) 646–651.

[39] L. J. Pyrak-Nolte, D. D. Nolte, Frequency dependence of fracture stiffness, Geophysical Research Letters 19 (3) (1992) 325–328.

[40] J. Dvorkin, G. Mavko, A. Nur, Squirt flow in fully saturated rocks, Geophysics 60 (1) (1995) 97–107.

[41] S. Maultzsch, M. Chapman, E. Liu, X. Y. Li, Modelling frequency-dependent seismic anisotropy in fluid-saturated rock with aligned fractures: implication of fracture size estimation from anisotropic measurements, Geophysical Prospecting 51 (5) (2003) 381–392.